Science of Remote Sensing 12 (2025) 100274

Contents lists available at ScienceDirect

Science of Remote Sensing

journal homepage: www.sciencedirect.com/journal/science-of-remote-sensing

PSO-optimized dual-channel BP neural network for bathymetric prediction using multisource marine geodetic data: A case study of the gulf of Mexico

Jiajia Yuan [a,*], Haoran Liu [a], Jianli Chen [b,c], Chen Yang [a]

[a] School of Geomatics, Anhui University of Science and Technology, Huainan, Anhui, China
[b] Department of Land Surveying and Geo-Informatics, The Hong Kong Polytechnic University, Hong Kong, China
[c] Research Institute for Land and Space, The Hong Kong Polytechnic University, Hong Kong, China

ARTICLE INFO

Keywords:
Bathymetric prediction
Particle swarm optimization
Backpropagation neural network
Gravity anomaly
Marine geophysical data integration

ABSTRACT

Accurate seafloor topography is essential for marine scientific research, resource exploration, and understanding geological processes. Traditional bathymetric surveying methods are constrained by limited spatial coverage and high operational costs, particularly in deep-sea environments. To overcome these challenges, we developed a Particle Swarm Optimization (PSO)-optimized dual-channel BP neural network (PSO_BP), integrating shipborne bathymetric data with satellite altimetry-derived gravity anomalies. These gravity anomalies were further decomposed into long-wavelength, short-wavelength, and residual components to enhance bathymetric prediction accuracy. We systematically evaluate the impact of different gravity data combinations, including gravity anomalies, gravity gradients, and vertical deflections, used individually, in pairs, or as a three-component combination, on bathymetric prediction accuracy. Results show that PSO_BP consistently outperforms existing models (GEBCO_2024, Topo_25.1, DTU18_BAT, and SRTM15 + V2.6), achieving the lowest RMSE (25.45 m), MAE (9.95 m), MAPE (3.70 %), and highest R^2 (99.96 %) across various depth ranges and shoreline distances. The decomposition of gravity anomalies into long- and short-wavelength components and their residuals proves to be the most effective approach for improving bathymetric prediction accuracy, while PSO optimization enhances model convergence and reduces prediction errors. This study highlights the importance of integrating diverse gravity datasets and advanced optimization techniques to improve the accuracy and robustness of seafloor depth prediction, offering a reliable solution for global bathymetric mapping in deep and remote ocean regions.

1. Introduction

Seafloor topographic mapping is fundamental to marine scientific research, offering essential data for marine resource exploration, tectonic analysis, sediment transport studies, and ocean circulation modeling (Li and Zhao, 2022; Zhou et al., 2023; Harper and Sandwell, 2024). Traditional methods, such as single-beam and multi-beam echo sounding systems have proven effective in shallow to moderate-depth regions. However, they face significant challenges in deep-sea environments due to limited spatial coverage, high operational costs, and difficulties in data acquisition (Xi et al., 2024). These limitations have motivated the search for more efficient and scalable approaches capable of generating high-resolution bathymetric data in remote and data-sparse areas.

Gravity anomaly-based methods have been widely adopted for seafloor topography prediction. The gravity geological approach estimates bathymetric profiles by combining gravity anomalies with geophysical and geological constraints and is particularly effective where direct measurements are unavailable (Ibrahim and Hinze, 1972; Xiang et al., 2017). Notably, the Smith and Sandwell method (1997) advanced global-scale mapping by integrating satellite altimetry data with marine gravity models, enhancing bathymetric resolution in uncharted ocean regions (Smith and Sandwell, 1997; Sandwell et al., 2014). Further improvements have been achieved using techniques such as simulated annealing, admittance function analysis, and nonlinear iterative least squares (Yang et al., 2018; Fan et al., 2020, 2021). However, many of these models rely on simplified linear assumptions, limiting their capacity to represent the complex nonlinear relationship between gravity signals and seafloor morphology—especially in geologically active or topographically complex areas (Annan et al.,

* Corresponding author.
E-mail address: yuanjiajia2008@126.com (J. Yuan).

https://doi.org/10.1016/j.srs.2025.100274
Received 15 April 2025; Received in revised form 29 June 2025; Accepted 17 August 2025
Available online 21 August 2025

2022; Xu et al., 2023; Harper and Sandwell, 2024).

Gravity anomalies are typically categorized by spatial frequency: long-wavelength anomalies correspond to large-scale tectonic and mantle structures, while short-wavelength anomalies reflect localized features such as bedrock undulations and fault systems (Smith and Sandwell, 1997; Sandwell and Smith, 2009; Altinoğlu et al., 2015; Hsiao et al., 2016). Effective bathymetric prediction requires the integration of gravity signals across multiple spatial scales to capture both global and local morphological characteristics (Yuan et al., 2025). Traditional gravity-based inversion techniques, however, often struggle to adequately incorporate this multi-scale information, underscoring the need for data-driven methods with stronger nonlinear modeling capabilities.

Deep learning techniques, particularly neural networks, have emerged as powerful tools for bathymetric prediction owing to their capability to capture complex nonlinear relationships and automatically learn multi-scale spatial features from heterogeneous data sources. These data-driven models minimize the dependence on predefined physical assumptions and demonstrate strong generalization performance across diverse oceanographic settings. Recent studies have successfully applied convolutional neural networks (CNNs) and multilayer perceptrons (MLPs) to predict seafloor depth using gravity anomaly and remote sensing data in the Gulf of Guinea and the Caribbean Sea, respectively (Annan and Wan, 2022; Zhou et al., 2024). In addition, random forest algorithms have achieved high predictive accuracy in optically shallow waters by leveraging multi-temporal satellite imagery (Sagawa et al., 2019). To enhance feature extraction, Ge et al. (2025) proposed a multi-channel convolutional neural network (MCCNN) that integrates multiple gravity-derived attributes for bathymetric modeling in the Northwest Pacific, underscoring the benefits of utilizing diverse spectral components of gravity signals. However, despite these advancements, the systematic integration of gravity anomalies at different spectral scales—such as long-wavelength and short-wavelength components, as well as their residuals—remains largely underexplored. Moreover, few studies have conducted comprehensive comparative evaluations of varying gravity data combinations to assess their relative contributions to predictive accuracy.

Among the available neural architectures, backpropagation (BP)-based networks have gained increasing traction due to their flexibility in approximating nonlinear mappings and spatial heterogeneity in seafloor topography (Zong et al., 2022; Sun et al., 2022; Wu et al., 2024). Nevertheless, training BP networks often suffers from intrinsic limitations such as vanishing gradients, slow convergence, and high sensitivity to weight initialization, which may adversely affect model robustness and generalization (Zhang et al., 2024).

To address these limitations, recent studies have primarily focused on two strategies: enhancing optimization algorithms and redesigning network architectures. Among various optimization methods, Particle swarm optimization (PSO) has emerged as a particularly effective approach due to its simplicity, efficiency, and strong global search capabilities (Kennedy and Russell, 2002; Gad, 2022). PSO mimics the collective behavior of birds or fish and has been successfully applied to a wide range of geophysical and engineering problems. For instance, it has been used to extract fault parameters from gravity data profiles (Essa et al., 2021), model magnetic anomalies in basement complexes (Ekwok et al., 2023), and interpret complex fault structures from vertical gravity profiles (Anderson et al., 2020), demonstrating its robustness in handling nonlinear inverse problems. In the energy sector, PSO has also been effectively adapted for load flow analysis in power systems (Mehfuz and Kumar, 2014), offering a faster and more flexible alternative to traditional numerical methods.

When integrated with BP neural networks, PSO accelerates convergence, mitigates sensitivity to initial weight settings, and enhances robustness against entrapment in local minima (Huang et al., 2020; Li, 2022; Song et al., 2023). These benefits make PSO particularly suitable for optimizing complex nonlinear models where traditional gradient-based approaches often struggle. In addition, other global optimization techniques, such as fast-simulated annealing (Gou et al., 2019) and genetic algorithms (Chen et al., 2023; Wu et al., 2024), have also demonstrated potential in improving training stability and avoiding local optima. However, among these, PSO stands out for its balance between global search ability and computational simplicity, making it a compelling choice in diverse application domains ranging from geophysical inversion to intelligent system modeling.

In addition to algorithmic optimization, redesigning the network architecture has proven critical. The dual-channel BP neural network is particularly effective for gravity anomaly processing, as it establishes independent pathways for short- and long-wavelength gravity anomalies, reducing spectral interference during feature fusion. This structure ensures that key features from different gravity components are accurately captured, enhancing the model's predictive capacity. Furthermore, cross-channel residual connections are introduced to enhance gradient stability, improving inversion accuracy in complex seafloor terrains (Sun et al., 2022). Although this architecture does not directly solve nonlinear optimization challenges, it significantly strengthens feature extraction and model robustness, leading to more accurate seafloor topography predictions.

In the present study, we propose a PSO-optimized dual-channel BP neural network (PSO_BP) for seafloor topography prediction. The model integrates shipborne bathymetric data with satellite altimetry-derived gravity anomalies—specifically long- and short-wavelength components and their residuals—to develop an accurate prediction framework for the Gulf of Mexico (80° W–100° W, 17° N–32° N). The focus is on optimizing learning rates to enhance model convergence, stability, and predictive accuracy. The model's performance is rigorously evaluated, aiming to provide an efficient and robust solution for complex seafloor mapping.

2. Research area and data

2.1. Research area

This study focuses on the Gulf of Mexico (80° W–100° W, 17° N–32° N), a marginal ocean basin located in the southeastern region of North America. The Gulf is partially enclosed by surrounding landmasses and exhibits an approximately oval shape, extending about 1609 km east to west and approximately 1287 km north to south, with a total area of approximately 1.55 million square kilometers. Bathymetrically, the region features substantial depth variation, ranging from shallow coastal waters of less than 10 m to deep-sea areas exceeding 4500 m. The average depth is approximately 1646 m, based on GEBCO_2024 data over the study area. This reflects the complex topography of the basin, including broad continental shelves and the Sigsbee Abyssal Plain. This wide depth range presents both challenges and opportunities for accurate seafloor modeling and inversion analysis.

2.2. Data

(1) Gravity Data: The gravity data used in this study are derived from the SIO V32.1 marine gravity model, provided by the Scripps Institution of Oceanography (SIO) at the University of California, San Diego, in 2022. This dataset was generated by processing radar altimetry measurements collected from multiple satellite missions. Sea surface height anomalies obtained from satellite altimeters were converted into gravity anomalies through geophysical inversion methods, from which vertical gravity gradients and vertical deflections (divided into east–west and north–south components) were subsequently calculated. All these gravity parameters are provided at a global grid resolution of 1 arc-minute (1′). The dataset is available at the following link: https://topex.ucsd.edu/pub/global_grav_1min (accessed March 16, 2025).

Fig. 1 illustrates the gravity data used in this study, with Fig. 1a showing gravity anomalies, Fig. 1b showing vertical gravity gradients, and Fig. 1c and d illustrating vertical deflections in the east–west and north–south directions, respectively. The white area in the upper-right corner indicates oceanic regions excluded from this study, while the remaining white areas represent land regions.

In this study, different combinations of gravity datasets—including individual, paired, or combined use of all three types—were employed as input features for seafloor topography prediction using the deep learning model. The predictive results from different combinations were compared to evaluate the model's performance in utilizing short- and long-wavelength gravity anomalies along with their residuals for seafloor depth prediction.

(2) Bathymetric Models: Several bathymetric models were employed in this study for accuracy evaluation, including GEBCO_2024, Topo_25.1, SRTM15 + V2.6, and DTU18_BAT. Additionally, the GEBCO_2024 model was utilized to select shipborne bathymetric points.

GEBCO_2024 is a global terrain model released in 2024 by the international oceanographic community, covering both oceanic and terrestrial regions. It integrates multiple data sources, including ship-based sonar measurements, satellite altimetry, and historical bathymetric surveys. With a grid resolution of 15 arc-seconds (approximately 500 m), GEBCO_2024 provides global ocean depth maps applicable to both deep-sea and shallow-water regions. Due to its high resolution and integration of diverse datasets, the model excels in resolving medium- and short-wavelength topographic features. The model is available for download at https://download.gebco.net/(accessed March 16, 2025).

Topo_25.1 is a global seafloor topography model developed by the SIO in 2023. It employs the Smith and Sandwell method (1997), integrating satellite altimetry with ship-based bathymetric measurements to generate a high-resolution seafloor grid. With a grid resolution of 1 arc-minute (approximately 1.85 km), Topo_25.1 offers improved detail over earlier models, particularly in resolving medium- and short-wavelength topographic features. This model effectively captures finer topographic signals, enhancing the precision of seafloor topography predictions. The dataset is available at https://topex.ucsd.edu/pub/global_topo_1min/(accessed March 16, 2025).

SRTM15 + V2.6 is a global seafloor topography model developed by the SIO in 2024. This model employs a machine learning approach, utilizing a neural network trained with the TensorFlow framework to integrate multiple data sources, including satellite altimetry, ship-based bathymetric measurements, and land topography data (Harper and Sandwell, 2024). With a grid resolution of 15 arc-seconds (approximately 500 m), it provides a detailed representation of both seafloor and land elevations. Compared to earlier versions, V2.6 significantly enhances accuracy and spatial coverage, particularly in regions with extensive multibeam data. The model is available for download at https://topex.ucsd.edu/pub/srtm15_plus/(accessed March 16, 2025).

DTU18_BAT is a global seafloor topography model developed by the Technical University of Denmark (DTU). It integrates satellite altimetry data with multibeam bathymetric measurements to produce a high-resolution and accurate seafloor model. With a grid resolution of 1 arc-minute (approximately 1.85 km), DTU18_BAT is suitable for both deep-sea and shallow-water research. The model demonstrates significant improvements over earlier versions in terms of data coverage and accuracy, particularly in areas with dense multibeam data. The dataset is available at https://ftp.space.dtu.dk/pub/DTU18/1_MIN/(accessed March 16, 2025).

(3) Shipborne Bathymetric Data: The shipborne bathymetric data utilized in this study were obtained from the National Centers for

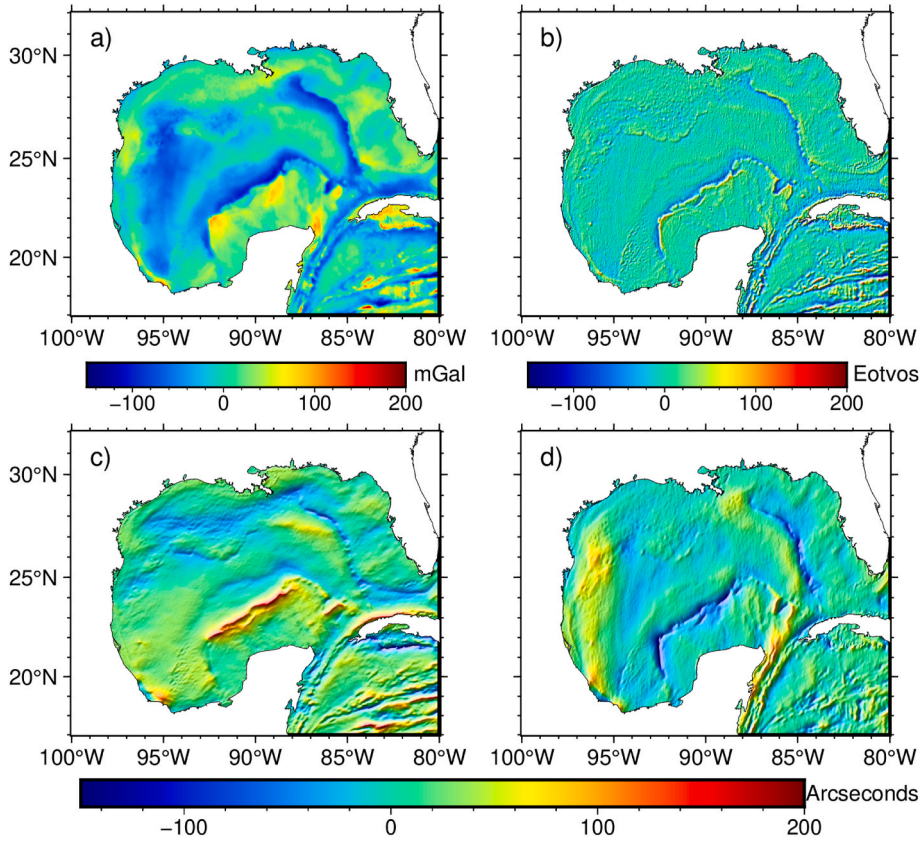

Fig. 1. Gravity data sets for the Gulf of Mexico region: (a) gravity anomalies, (b) vertical gravity gradients, (c) east–west vertical deflections, (d) north–south vertical deflections.

Environmental Information (NCEI) of the National Oceanic and Atmospheric Administration (NOAA). The dataset is accessible at the following link: https://www.ncei.noaa.gov/maps/trackline-geophysics (accessed March 16, 2025). A total of 1,378,927 data points was available within the study area. However, potential inaccuracies in the positioning and sounding precision of earlier datasets necessitated an initial screening process to ensure data quality.

Duplicate data points with identical latitude and longitude coordinates were identified and merged, where identical depth values were consolidated into a single entry to eliminate redundancy. Subsequently, the "3-Sigma Criteria" rule was applied, using the GEBCO_2024 model as a reference, to identify and remove anomalous data points. Specifically, bathymetric depths from the GEBCO_2024 model were interpolated at locations corresponding to the shipborne data points, and the differences between the interpolated depths and the measured shipborne depths were calculated. Data points with discrepancies exceeding three standard deviations were classified as outliers and subsequently excluded from the dataset. As a result, 12,390 data points were removed, representing approximately 0.9 % of the initial dataset. Following the filtering process, 1,366,537 shipborne bathymetric data points remained for subsequent analysis, as illustrated in Fig. 2.

To mitigate the risk of overfitting during model training and to construct a robust deep learning-based bathymetric inversion model, a 3:1:1 ratio was adopted for splitting the dataset into training, prediction, and validation points. Specifically, 819,923 data points were designated as training points, 273,307 as prediction points, and 273,307 as validation points. The dataset was partitioned using the train_test_split method (Vrigazova, 2021), following a sequential partitioning strategy to ensure consistency in data distribution.

In this sequential approach, the entire dataset was divided into multiple subsets, each containing five data points. Within each subset, the first, third, and fifth points were assigned as training points, the second as a prediction point, and the fourth as a validation point. If fewer than five points remained, the residual data points were directly assigned as training points.

The trainingpoints, comprising 60 % of the total data, were used for model training, ensuring enough samples for learning while maintaining good generalization performance. The remaining 40 % of the data were equally divided into prediction and validation points (20 % each). The prediction points were used to evaluate the model's performance on unseen data, while the validation points were employed to monitor accuracy and stability during training.

3. Methodology

3.1. Principle of the dual-channel BP neural network

The dual-channel BP neural network used in this study consists of an input layer, hidden layers, and an output layer, with each layer containing neurons that perform specific functions, as illustrated in Fig. 3.

The input layer receives six types of features: Longitude (LON), Latitude (LAT), Short-wavelength gravity anomalies (SG), Long-wavelength gravity anomalies (LG), Residual short-wavelength gravity anomalies (RSG), and Residual long-wavelength gravity anomalies (RLG). In addition to these six input features, the input layer also includes a bias term (b_j^l). The bias term is a trainable parameter that allows the activation function to shift, thereby enhancing the model's ability to fit the data and capture complex nonlinear relationships. These features are first flattened into one-dimensional arrays before being input into the network. Each neuron in the input layer, including the bias term, transmits these data to the subsequent layers for further processing.

The network comprises three hidden layers within each channel, performing complex computations and nonlinear transformations to extract features relevant to seafloor depth prediction. Each hidden layer consists of fully connected neurons arranged as follows: 64 neurons in the first layer, 128 neurons in the second layer, 256 neurons in the third layer. This hierarchical design adheres to the deep learning principle of progressive feature abstraction, whereby shallow layers capture low-level patterns and deeper layers integrate higher-order representations. The chosen node progression balances model capacity and computational efficiency, effectively accommodating the multi-scale characteristics of seafloor topography. Similar network configurations have demonstrated strong efficacy in geospatial data modeling, especially for nonlinear regression tasks involving gravity-topography relationships (Zhou et al., 2023; Sun et al., 2022).

Two parallel feature extraction channels are designed: the first channel processes feature from LON, LAT, LG, and RLG; the second channel processes feature from LON, LAT, SG, and RSG. This architecture is grounded in the geophysical principle that gravity signals exhibit scale-dependent characteristics: long-wavelength anomalies primarily reflect mantle dynamics and basin-scale tectonic processes, whereas short-wavelength anomalies are associated with localized seafloor morphology (Smith and Sandwell, 1997). By processing these spectrally distinct components through separate network channels, feature interference during backpropagation is effectively mitigated, enabling specialized weight optimization tailored to each spatial scale. Such scale-decoupled architectures are consistent with recent advances in marine gravity inversion methodologies (Annan et al., 2022; Sun et al., 2022; Yang et al., 2023). This design enables the model to accurately capture bathymetric variations across multiple spatial scales, thereby improving inversion performance and generalization.

The outputs from these two channels are concatenated into a unified feature vector, enhancing the model's ability to capture the intricate patterns in the data. During the forward propagation process, the output of j-th neuron y_j^l in the l-th layer is calculated as follows:

$$y_j^l = f\left(\sum_i w_{ji}^l x_i^{l-1} + b_j^l\right) \tag{1}$$

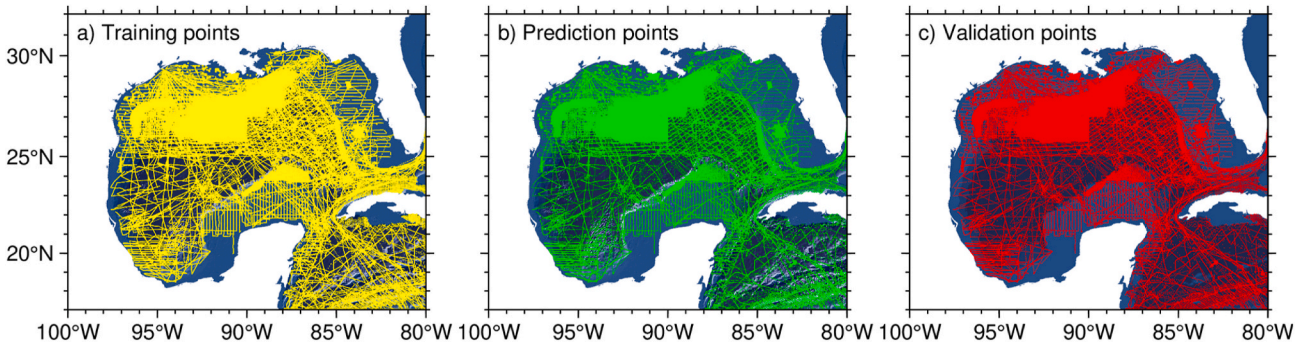

Fig. 2. Study area and distribution of shipborne bathymetric survey tracks (base map: GEBCO_2024), a) training points, b) prediction points, c) validation points.

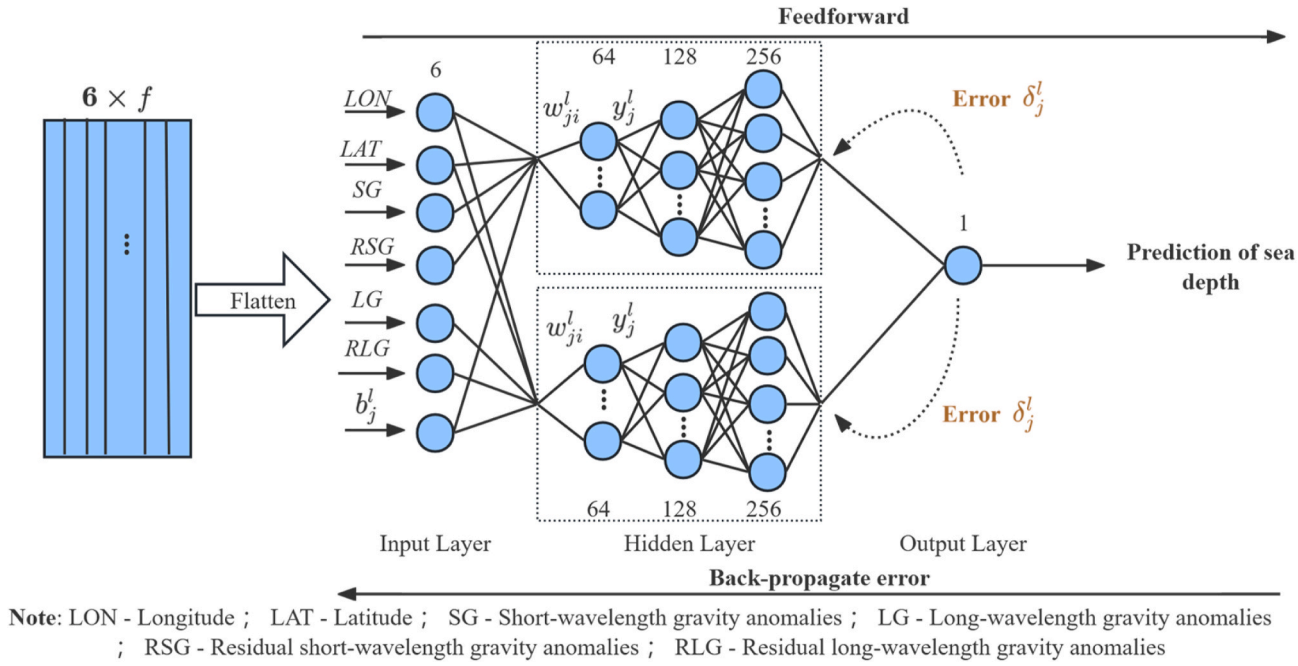

Fig. 3. Architecture of the dual-channel BP neural network for seafloor depth prediction.

Where w_{ji}^{l} is the weight connecting the i-th neuron in layer $l-1$ to the j-th neuron in layer l; x_i^{l-1} is the output from th e i-th neuron in the previous layer; b_j^l is the bias term for the j-th neuron in the l-th layer; f is the activation function (Rectified Linear Unit in this study). The bias term ensures that even when the weighted sum of inputs is zero, the neuron can still produce a non-zero output, enhancing the network's ability to fit complex seafloor topography data.

During training, the network adjusts its weights and biases by backpropagating the error from the output layer. The weight and bias updates are performed according to the gradient descent principle, ensuring that the prediction error is progressively minimized. The weight w_{ji}^{l} and bias term b_j^l are updated using the following formula, respectively:

$$w_{ji}^{l+1} = w_{ji}^{l} - \tau \frac{\partial L}{\partial w_{ji}^{l}} \tag{2}$$

$$b_{ji}^{l+1} = b_{ji}^{l} - \tau \frac{\partial L}{\partial b_{ji}^{l}} \tag{3}$$

Where τ is the learning rate, L is the loss function (Huber loss in this study), $\frac{\partial L}{\partial w_{ji}^{l}}$ and are $\frac{\partial L}{\partial b_{ji}^{l}}$ the partial derivatives of the loss function with respect to the weights and biases, respectively.

The activation function plays a key role in network performance by introducing nonlinearity, allowing it to model complex relationships. Given the nonlinear nature of seafloor topography, capturing the relationship between input features and depth is essential (Zhou et al., 2023). This study adopts the Rectified Linear Unit (ReLU) for its simplicity, computational efficiency, and ability to mitigate the vanishing gradient problem. For optimization, the Huber loss function was chosen, as it balances squared and absolute errors, making the model robust to both small and large prediction discrepancies.

To enhance training efficiency and generalization, a learning rate scheduler dynamically adjusts the learning rate, halving it if the validation loss stagnates for five epochs. An early stopping mechanism with a patience value of 10 prevents overfitting by halting training when no improvement is observed for 10 consecutive epochs. The best-performing model is retained, ensuring optimal performance on unseen data.

3.2. Particle Swarm Optimization (PSO) algorithm

The PSO algorithm is a population-based stochastic optimization technique inspired by the collective movement of birds and fish. As shown in Fig. 4, it explores a multi-dimensional search space using a swarm of particles, each representing a candidate solution. A particle's position denotes its current solution, while its velocity determines its movement toward a better solution. The algorithm iteratively updates each particle's position and velocity based on two key factors: the Personal Best (pBest), which denotes the best solution it has achieved thus far, and the Global Best (gBest), representing the best solution identified by any particle in the swarm. The position and velocity updates follow these equations:

$$v_i^d(t+1) = w \cdot v_i^d(t) + c_1 \cdot r_1 \cdot \left(\mathrm{pBest}_i^d - x_i^d(t)\right) + c_2 \cdot r_2 \cdot \left(\mathrm{gBest}_i^d - x_i^d(t)\right) \tag{4}$$

$$x_i^d(t+1) = x_i^d(t) + v_i^d(t+1) \tag{5}$$

Where, $v_i^d(t+1)$ is the updated velocity of particle i in dimension d at iteration $t+1$; w is the inertia weight, controlling the balance between exploration and exploitation; c_1 and c_2 are the cognitive and social coefficients, influencing how much a particle is attracted to its own best position and the global best position, respectively; r_1 and r_2 are random numbers in the range [0,1] to introduce stochasticity in the search process; pBest_i^d and gBest_i^d represent the personal best and global best positions of particle i in dimension d, respectively; $x_i^d(t+1)$ is the updated position of particle i in dimension d at iteration $t+1$.

To ensure the effective performance of the PSO algorithm, appropriate parameter configuration is essential. In this study, proper tuning of w, c_1 and c_2 are carefully tuned to balance global exploration and local exploitation. Specifically, the inertia weight w controls the impact of a particle's previous velocity on its current motion, where a larger w promotes global search and a smaller w encourages local refinement. The coefficients c_1 and c_2 govern the influence of the particle's personal best and the global best positions, respectively. A higher c_1 encourages individual exploration, while a higher c_2 promotes convergence toward

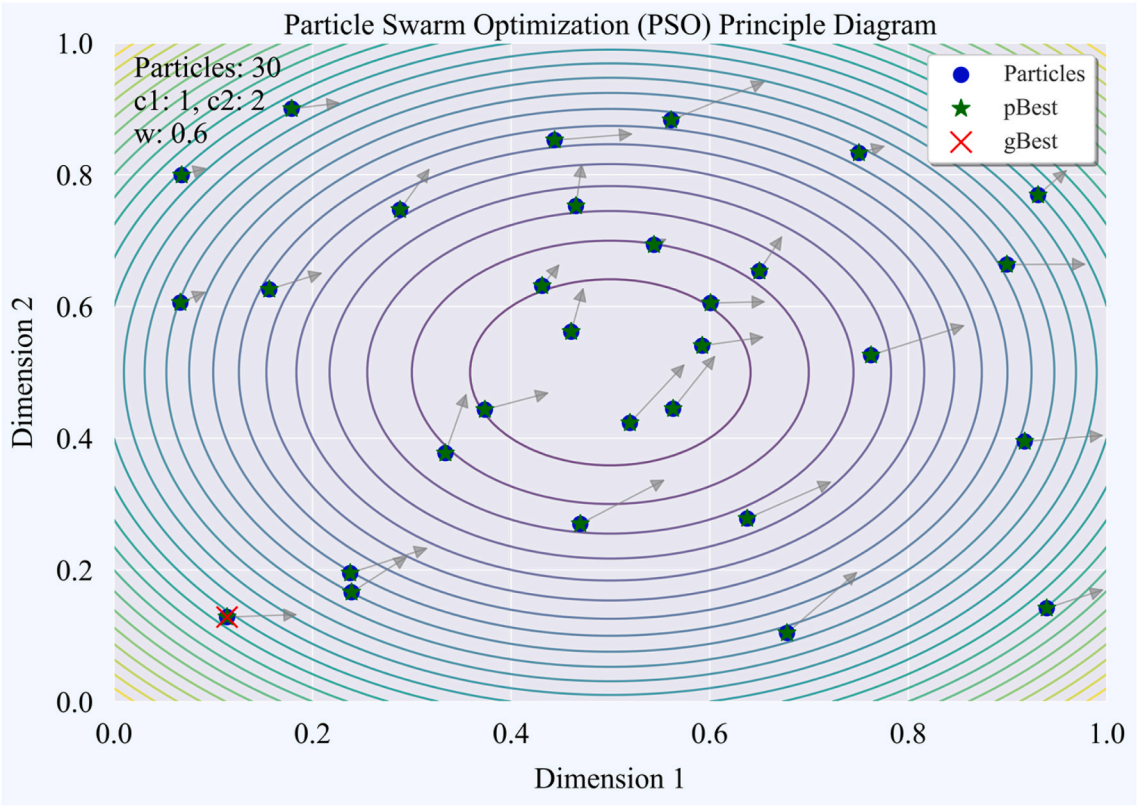

Fig. 4. Particle Swarm Optimization (PSO) principle diagram illustrating particle positions, pbest, gbest, and velocity directions.

the swarm's best-known position.

Based on extensive empirical experiments and reference to prior optimization studies, we selected $w = 0.6, c_1 = 1,$ and $c_2 = 2$ as the optimal configuration for our application. This setting was found to provide a desirable trade-off between convergence speed and solution quality. Additionally, the swarm size was set to 30 particles, which balances computational efficiency with sufficient diversity for effective search. As shown in Fig. 4, the swarm consists of 30 particles, each randomly initialized to represent a possible configuration of network weights and biases.

To prevent premature convergence and maintain diversity within the swarm, we implemented two essential strategies: velocity clamping and position boundary constraints. In our implementation, velocity clamping is used to restrict the maximum speed at which a particle can move in each dimension. The upper bound for velocity is set to a fixed proportion (typically 10 %–20 %) of the corresponding dimension's search range. This proportional threshold prevents particles from making excessively large movements that might cause them to overshoot optimal regions or destabilize the optimization process. By constraining particle velocity in this way, we ensure a smoother search trajectory and reduce the risk of erratic or divergent behavior. Additionally, position boundary constraints are applied to ensure that all particles remain within the predefined search space. After each position update, we check whether any particle exceeds the allowed boundaries in any dimension. If it does, its position is adjusted by setting it directly to the nearest boundary value. This clipping strategy guarantees that every particle remains in a valid solution space, thus preserving the feasibility and stability of the optimization process. Together, these two mechanisms help balance the global and local search behavior of the algorithm, improve solution robustness, and prevent convergence to suboptimal solutions.

In this study, PSO is applied to optimize the weights and biases of a dual-channel BP neural network for seafloor depth prediction. Unlike traditional gradient-based training, which often suffers from local minima and slow convergence, PSO enables a global search that improves both training efficiency and prediction accuracy. The model effectively addresses inversion stability challenges by mitigating ill-posedness through spectral decoupling, preventing overfitting via swarm optimization, and enhancing noise resilience through residual components, thus enabling reliable predictions in complex marine environments. By leveraging swarm intelligence, PSO systematically refines the network parameters, ensuring a more effective learning process.

To achieve optimal performance, it is essential to accurately evaluate each candidate solution during the optimization process. We define a fitness function based on a weighted sum of absolute differences across three key metrics—mean, STD, and RMSE. This fitness function guides the swarm toward configurations that not only minimize prediction errors but also enhance model stability and generalization. During optimization, each particle updates its personal best (pBest), while the swarm collectively refines the global best (gBest), iteratively improving the network's predictive capability.

3.3. Seafloor topography prediction using PSO-optimized dual-channel BP neural network

Fig. 5 presents the overall workflow for predicting seafloor topography using a PSO-optimized BP neural network, covering four key stages: data preprocessing, network training, prediction, and output results.

3.3.1. Data preprocessing

① Gravity anomaly feature extraction:

The short-wavelength gravity anomaly is first calculated at NCEI training points using the Burgi board formula, which estimates the gravitational effect of the seafloor's mass distribution. The formula is

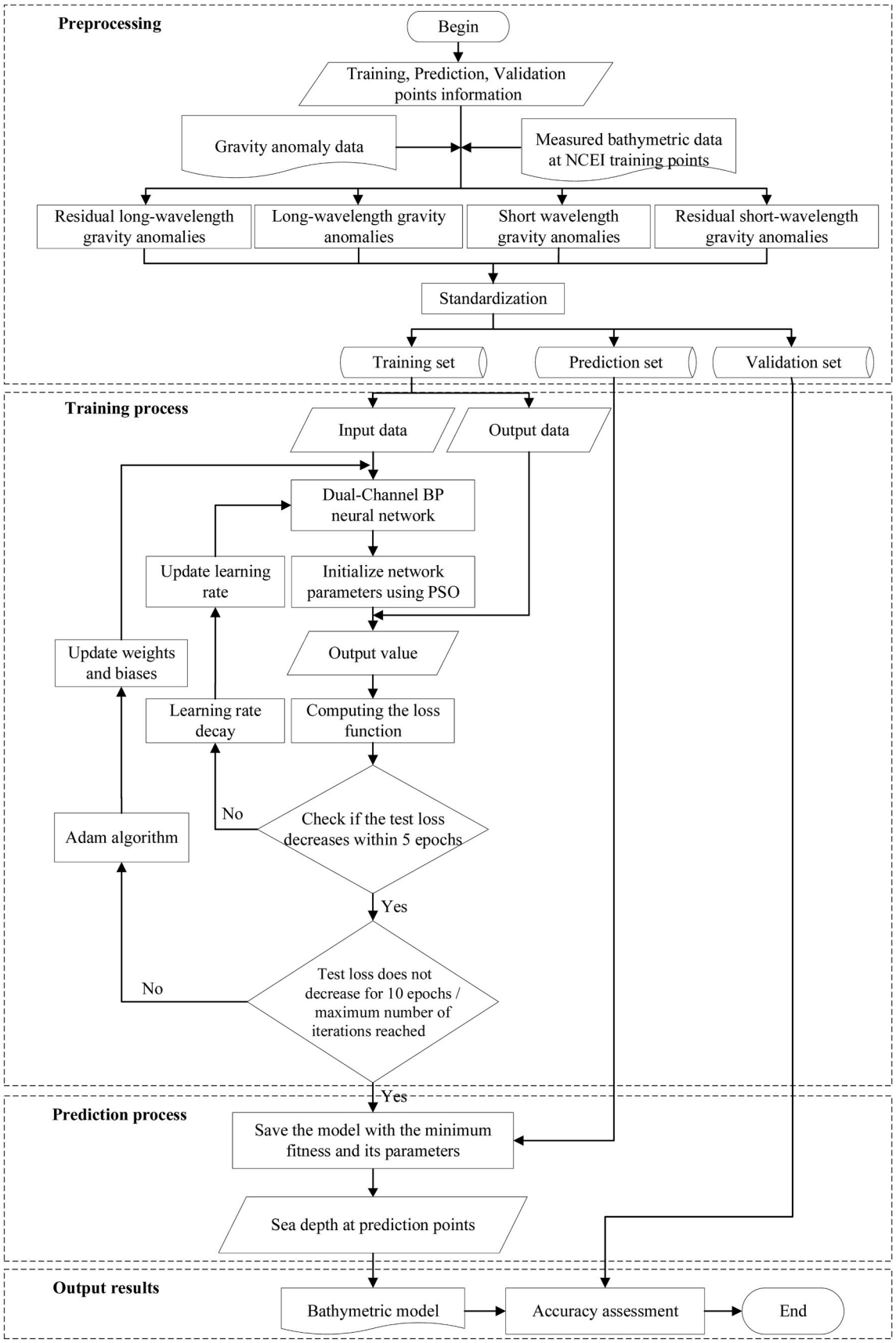

Fig. 5. Workflow for seafloor topography prediction using PSO-optimized dual-channel BP neural network.

expressed as:

$$\Delta g_{short}(j) = 2\pi G \Delta\rho (E(j) - D) \tag{6}$$

Where $\Delta g_{short}(j)$ represents the short-wavelength gravity anomaly data at the j-th NCEI training point; G is the gravitational constant; $\Delta\rho$ is density contrast between seawater and bedrock, calculated using an iterative method based on shipborne depth measurements, with a final value of 1.092 g/cm^3 applied in this study; $E(j)$ is the seafloor depth at the j-th NCEI trainingpoint; and D is the reference depth, determined by the maximum seafloor depth within the study area and set to −7275 m.

Subsequently, the long-wavelength gravity anomalys $\Delta g_{long}(j)$ at NCEI trainingpoint j is calculated by subtracting the $\Delta g_{short}(j)$ from the gravity anomaly derived from the SIO V32.1 gravity anomaly model, as follows:

$$\Delta g_{long}(j) = \Delta g_{obs}(j) - \Delta g_{short}(j) \tag{7}$$

Based on the long-wavelength gravity anomalies obtained at NCEI trainingpoints, the tension-adjusted continuous curve interpolation method is applied to estimate the long-wavelength gravity anomalies at NCEI prediction points (Xiang et al., 2017). The short-wavelength gravity anomalies at these prediction points are then calculated by subtracting the interpolated long-wavelength gravity anomalies from the gravity anomalies derived from the SIO V32.1 gravity anomaly model.

Once both short- and long-wavelength gravity anomaly data are obtained, a linear regression model is employed to establish the relationship between shipborne depth measurements and gravity anomalies. The regression slopes for the long-wavelength and short-wavelength anomalies are −0.032 mGal/m and 0.046 mGal/m, respectively. Based on these slopes and the corresponding shipborne depth measurements, reference values for both gravity anomalies are calculated. The residual long- and short-wavelength gravity anomalies are then derived by subtracting these reference values from the computed anomalies (An et al., 2022, 2024).

② Data Standardization:

All extracted features—including longitude, latitude, long- and short-wavelength gravity anomalies, and their residuals—are standardized to have a mean of 0 and a standard deviation of 1. This ensures consistent scaling for input into the Dual-Channel BP Neural Network. The standardizedformula is

$$\acute{x} = \frac{x - \mu}{\sigma} \tag{8}$$

Where, $\acute{x}$ is the standardizedvalue, x is the original value, μ is the mean of the original data, and σ is the standard deviation of the original data. After standardized, all feature data are classified into training, prediction, and validation sets based on their correspondence to training, prediction, or validation points.

3.3.2. Training process

The standardizedtraining data are fed into the dual-channel BP neural network, where PSO initializes the weights and biases. The network iteratively calculates training and test losses by comparing predicted and actual seafloor depths. If the test loss fails to improve for 5 epochs, the learning rate is halved to enhance convergence. Training stops after 200 epochs or if the test loss remains unchanged for 10 consecutive epochs. To ensure optimal parameter updates, the Adam algorithm is used for weight and bias adjustments. After each iteration, the model is saved for fitness evaluation, and the model with the lowest fitness value is selected for final seafloor depth prediction.

3.3.3. Prediction

During the prediction phase, the deep learning model trained using the training points is applied to estimate seafloor depths at the prediction points. Specifically, the model uses the parameters learned during training to process the prediction data in the same manner. Input features—including longitude, latitude, long- and short-wavelength gravity anomalies, and their residuals—are fed into the trained neural network. To ensure prediction consistency and accuracy, the input feature order strictly follows that used during training. The resulting predicted depths are then used to construct the bathymetric model of the Gulf of Mexico.

3.3.4. Model establishment

In this study, the model's accuracy is assessed using the following metrics: RMSE, mean absolute error (MAE), and coefficient of determination (R^2), and mean absolute percentage error (MAPE). The RMSE measures the square root of the average squared differences between predicted and actual values. It is sensitive to outliers, and a smaller value indicates higher prediction accuracy. The MAE reflects the average magnitude of prediction errors, with lower values indicating better model accuracy and robustness to random noise and outliers (Hodson, 2022). The MAPE provides depth-normalized relative error assessment as a percentage of actual depth, complementing absolute metrics especially in deeper zones where larger absolute errors may correspond to smaller relative deviations (Zhou et al., 2023). The R^2 metric indicates how well the predicted values match the actual data, with a value closer to 1 representing a better model fit (Chicco et al., 2021).

The formula for the MAE, R^2, and MAPE metrics are defined as follows:

$$\mathrm{MAE} = \left(\sum_{i=1}^{n} |y_i - \widehat{y}_i|\right) \Big/ n \tag{8}$$

$$R^2 = \left(1 - \frac{\sum_{i=1}^{n} (y_i - \widehat{y}_i)^2}{\sum_{i=1}^{n} (y_i - \overline{y})^2}\right) \times 100\% \tag{9}$$

$$\mathrm{MAPE} = \left(\sum_{i=1}^{n} \left|\frac{y_i - \widehat{y}_i}{y_i}\right|\right) \Big/ n \times 100\% \tag{10}$$

Where, n represents the number of samples; y_i represents the actual value of the i-th sample; $\widehat{y}_i$ represents the predicted value of the i-th sample,and $\overline{y}$ is the mean of the actual values.

4. Results and analysis

4.1. Seafloor topography model

Fig. 6 illustrates the PSO_BP seafloor model of the Gulf of Mexico. The northern and western regions are characterized by broad continental shelf areas with relatively shallow depths. The central region features an extensive abyssal plain, marked by a relatively flat seafloor at significant depths, with some localized seafloor undulations. The southeastern region is distinguished by greater depths and steeper slope variations, though prominent ridges are less common. Additionally, submarine canyons may be present along the continental slope regions, formed by erosion from ocean currents and recognized as significant geomorphological features.

4.2. Comparison with existing models

To quantitatively evaluate the accuracy and consistency of the PSO_BP model in seafloor depth prediction, it is compared against the GEBCO_2024, Topo_25.1, DTU18_BAT, and SRTM15 + V2.6 models using RMSE, MAE, R^2 and MAPE as evaluation metrics. All models were interpolated to the NCEI validation points, and the statistical comparison is summarized in Table 1. Among the evaluated models, the PSO_BP

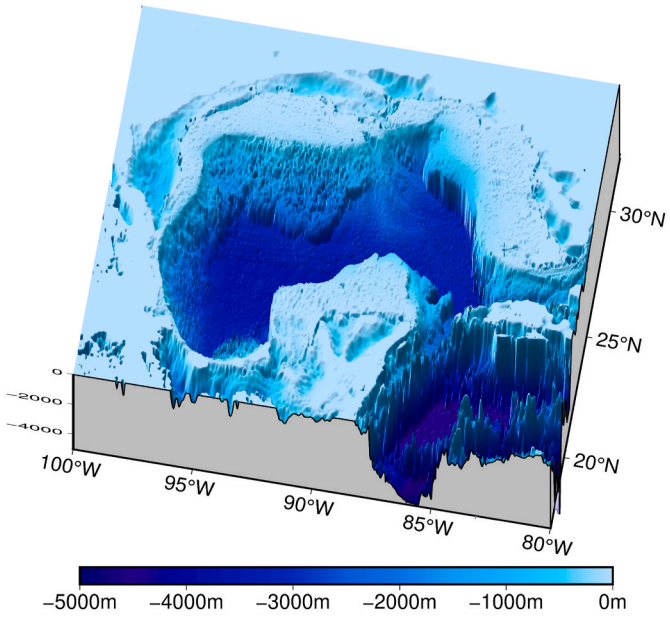

Fig. 6. PSO_BP seafloor model of the Gulf of Mexico.

Table 1
Statistical Results of the Comparison of GEBCO_2024, Topo_25.1, DTU18_BAT, SRTM15 + V2.6, and PSO_BP with Measured Bathymetric Data at NCEI Validation Points (Unit: m).

Model	Mean	STD	RMSE	MAE	R^2/%	MAPE/%
PSO_BP	0.08	25.45	25.45	9.95	99.96	3.70
GEBCO_2024	2.69	30.08	30.20	15.28	99.94	6.97
Topo_25.1	−1.54	36.80	36.84	15.39	99.91	11.65
DTU18_BAT	0.22	54.73	54.73	21.09	99.80	8.06
SRTM15 + V2.6	−0.08	33.22	33.22	13.03	99.93	6.14

model exhibits the best overall performance. It achieves the lowest RMSE of 25.45 m, outperforming GEBCO_2024 (30.20 m), Topo_25.1 (36.84 m), DTU18_BAT (54.73 m), and SRTM15 + V2.6 (33.22 m), indicating higher prediction accuracy with minimal overall error. In terms of MAE, PSO_BP again yields the lowest value (9.95 m), substantially better than GEBCO_2024 (15.28 m), Topo_25.1 (15.39 m), DTU18_BAT (21.088 m), and SRTM15 + V2.6 (13.03 m), reflecting its enhanced precision and reduced average deviation. Regarding R^2, PSO_BP achieves the highest score of 99.96 %, slightly surpassing GEBCO_2024 (99.94 %), Topo_25.1 (99.91 %), DTU18_BAT (99.80 %), and SRTM15 + V2.6 (99.93 %), demonstrating its stronger capability to capture the variance of observed bathymetric data. Additionally, the MAPE of PSO_BP is 3.70 %, notably lower than all other models, further confirming its robustness and reliability in predictive performance.

Fig. 7 compares the prediction errors of PSO_BP, GEBCO_2024, Topo_25.1, DTU18_BAT, and SRTM15 + V2.6 against measured bathymetric data at NCEI validation points, using histograms to illustrate error distribution and scatter plots to show depth-related variability. As shown in Fig. 7, PSO_BP (a) exhibits the most concentrated error distribution, with the majority of differences tightly clustered within ±50 m, forming a sharp-peaked histogram with minimal spread, indicating high accuracy and low variability. The scatter plot confirms this stability, showing minimal error dispersion across all depths, suggesting that PSO_BP maintains consistent performance regardless of depth. In contrast, GEBCO_2024 (b) has a slightly broader error distribution, with most errors still within ±50 m, though with a longer tail, indicating occasional larger deviations. Its scatter plot reveals a gradual increase in error dispersion with depth, suggesting a slight decline in accuracy at greater depths. Topo_25.1 (c) and DTU18_BAT (d) exhibit further error expansion, as their histograms show a wider distribution, with a notable increase in the proportion of errors exceeding ±50 m, implying reduced prediction accuracy and increased variability. Their scatter plots confirm this trend, showing progressively increasing error dispersion at greater depths, indicating growing instability in deeper waters. SRTM15 + V2.6 (e) has the broadest error distribution, with the highest proportion of errors surpassing ±50 m. Its flatter histogram reflects significant variability and the lowest prediction accuracy, while its scatter plot reveals substantial error dispersion, particularly at greater depths, demonstrating high instability and unreliable performance in deep-sea regions.

To evaluate the influence of shoreline distance on model accuracy, a statistical comparison of PSO_BP, GEBCO_2024, Topo_25.1, DTU18_BAT, and SRTM15 + V2.6 was conducted using measured bathymetric data at NCEI validation points across varying offshore distances. Table 2 presents the results, showing that PSO_BP consistently delivers the highest accuracy and stability across all distance categories. At distances greater than 10 km, PSO_BP achieves the lowest STD and RMSE (both 27.37 m), significantly outperforming GEBCO_2024 (31.92 m), Topo_25.1 (39.08 m), DTU18_BAT (57.77 m), and SRTM15 + V2.6 (35.58 m). Its MAE is also the smallest (11.19 m), and its R^2 value is the highest (99.95 %), indicating strong consistency and minimal error variability. Moreover, PSO_BP shows the lowest MAPE (1.90 %), further confirming its superior relative accuracy compared to the other models, whose MAPE values range from 2.78 % (SRTM15 + V2.6) to 4.31 % (DTU18_BAT).

As the distance from the coastline increases (>20 km to >90 km), PSO_BP continues to outperform all other models. It maintains the lowest STD and RMSE values (ranging from 27.97 m to 28.94 m) and the lowest MAE (from 11.66 m to 12.48 m), while its R^2 remains consistently high (between 99.94 % and 99.95 %), demonstrating strong predictive stability across offshore regions. Importantly, PSO_BP also maintains the lowest MAPE at all distance categories (from 1.62 % at >20 km to 1.37 % at >90 km), while MAPE values for other models either remain above 2 % or increase with distance—indicating reduced precision and growing relative error. In contrast, while GEBCO_2024 and SRTM15 + V2.6 exhibit relatively stable performance, they consistently show higher STD, RMSE, MAE, and MAPE values than PSO_BP across all distances. Topo_25.1 and DTU18_BAT display notable performance degradation in deeper offshore regions (>60 km), with increasing variability, decreasing R^2, and MAPE values exceeding 2.6 % and even 4 % in some cases, reflecting reduced reliability in those areas. This comprehensive analysis highlights that PSO_BP outperforms all other models not only in terms of absolute error metrics (STD, RMSE, MAE) but also in relative accuracy (MAPE) and model consistency (R^2), making it a robust and reliable solution for bathymetric prediction across varying offshore distances.

To analyze how model prediction accuracy varies with increasing water depth, a comparative analysis was conducted using the PSO_BP, GEBCO_2024, Topo_25.1, DTU18_BAT, and SRTM15 + V2.6 models, with measured shipborne bathymetric data at NCEI validation points. Data were categorized into four distinct depth ranges (0–500 m, 500–1000 m, 1000–2000 m, and ≥2000 m) to assess each model's adaptability and accuracy under varying depth conditions. The statistical results are presented in Table 3.

Across all depth ranges, PSO_BP consistently demonstrates superior prediction accuracy. It achieves the lowest overall RMSE values (ranging from 9.94 m to 39.33 m) and MAE values (ranging from 2.99 m to 16.82 m), significantly outperforming the other models. In contrast, DTU18_BAT exhibits the largest errors, with RMSE and MAE values increasing notably with depth, reaching 93.33 m and 39.13 m, respectively, in depths ≥2000 m. Similarly, Topo_25.1 and SRTM15 + V2.6 show progressively larger prediction errors with increasing depth, though their errors remain less pronounced compared to DTU18_BAT. In terms of consistency, PSO_BP maintains the highest R^2 values across all depth ranges, consistently exceeding 99 %, which reflects its robust predictive

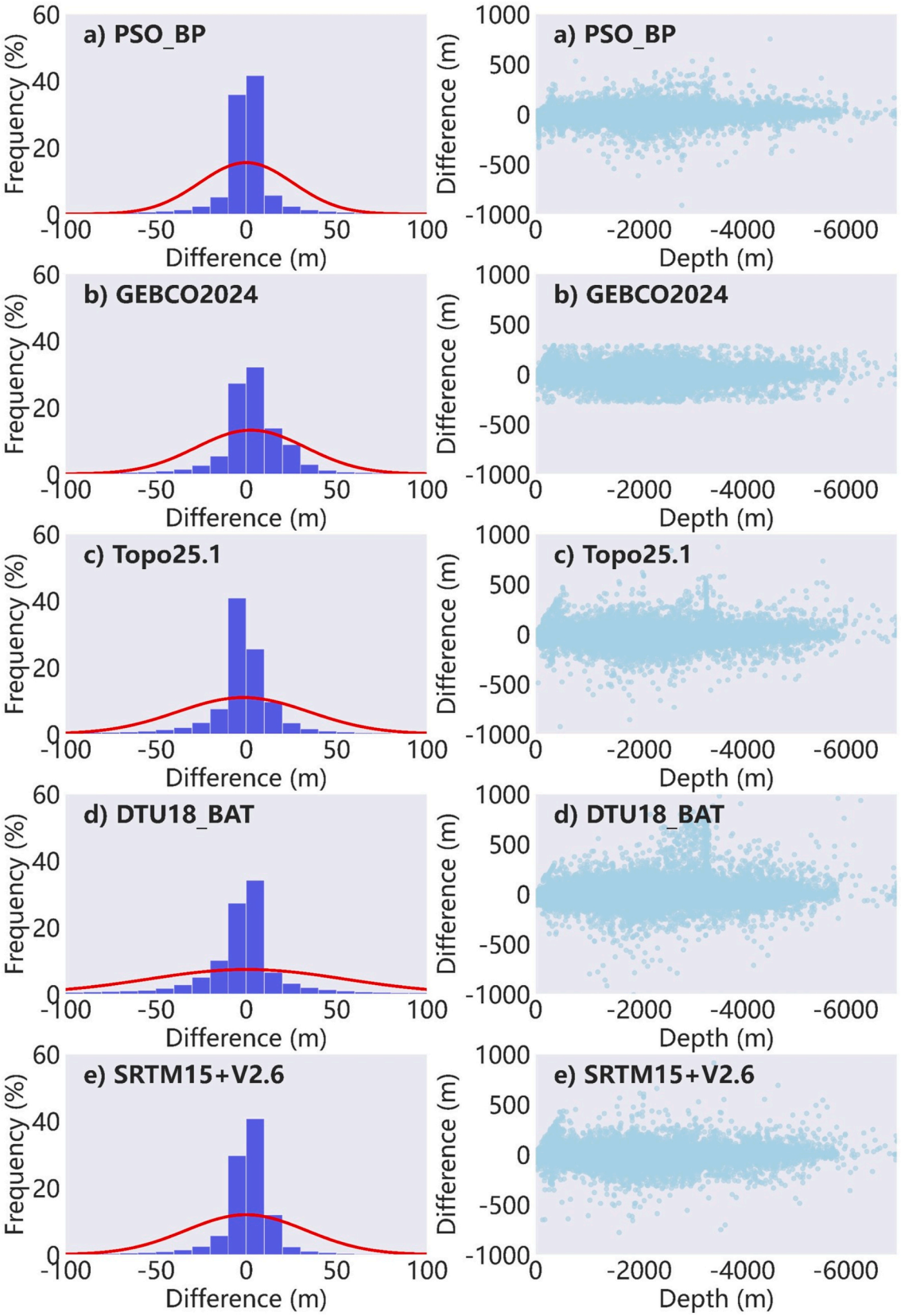

Fig. 7. Histograms (left) show the differences between the PSO_BP, GEBCO_2024, Topo_25.1, DTU18_BAT, and SRTM15 + V2.6 models and measured bathymetric data at NCEI validation points, with red lines indicating normal distribution curves; scatter plots (right) visualize model performance by illustrating differences across depth ranges.

Table 2
Statistical results of the comparison of GEBCO_2024, Topo_25.1, DTU18_BAT, SRTM15 + V2.6, and PSO_BP with measured bathymetric data at NCEI validation points across different shoreline distances (Unit: m).

Offshore distance (Validation points)	Model	Mean	STD	RMSE	MAE	R^2/%	MAPE/%
>10 km (242,312)	PSO_BP	0.10	27.37	27.37	11.19	99.95	1.90
	GEBCO_2024	2.94	31.92	32.05	17.04	99.93	3.05
	Topo_25.1	−1.55	39.08	39.11	17.07	99.89	3.94
	DTU18_BAT	0.10	57.77	57.77	23.52	99.77	4.31
	SRTM15 + V2.6	−0.25	35.58	35.58	14.50	99.91	2.78
>20 km (229,163)	PSO_BP	0.10	27.97	27.97	11.66	99.95	1.62
	GEBCO_2024	3.04	32.49	32.63	17.69	99.93	2.64
	Topo_25.1	−1.53	36.07	36.07	15.01	99.89	3.00
	DTU18_BAT	0.02	59.06	59.06	24.43	99.76	3.25
	SRTM15 + V2.6	−0.31	36.07	36.07	15.01	99.91	2.39
>30 km (220,568)	PSO_BP	0.10	28.35	28.35	11.95	99.94	1.56
	GEBCO_2024	3.09	32.83	32.97	18.06	99.92	2.48
	Topo_25.1	−1.53	40.07	40.10	18.04	99.89	2.65
	DTU18_BAT	0.06	59.84	59.84	24.96	99.75	2.95
	SRTM15 + V2.6	−0.33	36.35	36.35	15.30	99.91	2.24
>60 km (203,202)	PSO_BP	0.11	28.67	28.67	12.24	99.94	1.46
	GEBCO_2024	2.81	32.72	32.84	18.09	99.92	2.18
	Topo_25.1	−1.58	40.14	40.17	18.27	99.88	2.31
	DTU18_BAT	0.29	60.43	60.43	25.47	99.73	2.76
	SRTM15 + V2.6	−0.40	36.06	36.06	15.34	99.91	1.97
>90 km (183,088)	PSO_BP	0.12	28.94	28.94	12.48	99.94	1.37
	GEBCO_2024	2.02	32.59	32.65	17.93	99.92	1.99
	Topo_25.1	−2.03	40.82	40.87	18.62	99.88	2.19
	DTU18_BAT	0.93	60.80	60.90	25.74	99.72	2.60
	SRTM15 + V2.6	−0.88	36.44	36.45	15.45	99.90	1.87

Table 3
Statistical results of the comparison of GEBCO_2024, Topo_25.1, DTU18_BAT, SRTM15 + V2.6, and PSO_BP with measured bathymetric data at NCEI validation points across different depth ranges (Unit: m).

Depth (Validation Points)	Model	Mean	STD	RMSE	MAE	R^2/%	MAPE/%
0–500 m (110,632)	PSO_BP	−0.26	9.934	9.94	2.99	99.44	7.87
	GEBCO_2024	2.55	13.21	13.46	5.41	98.33	15.25
	Topo_25.1	−1.42	17.13	17.19	5.84	98.33	27.02
	DTU18_BAT	−0.84	15.23	15.25	6.13	98.69	13.59
	SRTM15 + V2.6	0.52	16.83	16.84	4.98	98.40	17.28
500–1000 m (26,429)	PSO_BP	−0.49	21.47	21.48	11.25	97.92	1.51
	GEBCO_2024	7.41	27.09	28.09	17.98	96.44	2.41
	Topo_25.1	−1.14	30.42	30.44	15.92	95.82	2.17
	DTU18_BAT	−5.23	36.57	36.94	22.23	93.84	2.98
	SRTM15 + V2.6	1.66	28.80	28.84	13.43	96.24	1.83
1000–2000 m (69,176)	PSO_BP	−0.62	28.38	28.39	14.17	99.01	0.98
	GEBCO_2024	4.46	34.66	34.94	21.42	98.51	1.51
	Topo_25.1	−0.71	37.79	37.80	20.08	98.25	1.38
	DTU18_BAT	−3.54	48.28	48.41	27.05	97.13	1.88
	SRTM15 + V2.6	1.40	34.23	34.26	16.56	98.56	1.15
≥2000 m (67,070)	PSO_BP	1.22	39.31	39.33	16.82	99.74	0.60
	GEBCO_2024	−1.12	43.64	43.65	24.40	99.67	0.87
	Topo_25.1	−2.97	55.80	55.88	26.17	99.47	0.91
	DTU18_BAT	7.73	93.01	93.33	39.13	98.51	1.34
	SRTM15 + V2.6	−3.50	50.22	50.34	22.65	99.57	0.78

stability regardless of depth variation. Other models, particularly DTU18_BAT, show a decline in R^2 values with increasing depth, indicating greater variability and reduced reliability in deeper waters. With regard to relative error, PSO_BP also achieves the lowest MAPE values across all depth intervals, decreasing from 7.87 % in shallow waters to only 0.60 % in depths ≥2000 m. This consistently low MAPE further confirms the model's strong generalization ability and suitability for bathymetric prediction across diverse marine environments. The results clearly highlight the superior adaptability and accuracy of the PSO_BP model across varying depth conditions. It maintains low prediction errors and high consistency, particularly in deep-water environments where other models exhibit greater variability and reduced precision.

4.3. Experiments with different input parameters

In recent years, deep learning algorithms have been increasingly applied to integrate diverse gravity data types for seafloor depth prediction, demonstrating notable improvements in model performance (Sun et al., 2022; Yang et al., 2023; Zhang et al., 2024; Zhou et al., 2024). To investigate whether incorporating multiple gravity data types—from single to multiple combinations—enhances prediction accuracy, and to assess the impact of PSO optimization on model performance, a series of experiments were designed using the dual-channel BP neural network and its PSO-optimized variant, as detailed in Table 4.

The selected gravity data types include short-wavelength gravity anomaly (SG), long-wavelength gravity anomaly (LG), residual short-

Table 4
Experimental setup. The input parameters include LON, LAT, SG, LG, RSG, RLG, GA, VGG, EVD and NVD.

Method	Case	Input parameters
BP	Case0	LON、LAT、SG、LG、RSG、RLG
	Case1	LON、LAT、GA
	Case2	LON、LAT、GA、VGG
	Case3	LON、LAT、GA、VGG、EVD、NVD
PSO_BP	Case4	LON、LAT、SG、LG、RSG、RLG
	Case5	LON、LAT、GA
	Case6	LON、LAT、GA、VGG
	Case7	LON、LAT、VGG
	Case8	LON、LAT、EVD、NVD
	Case9	LON、LAT、GA、EVD、NVD
	Case10	LON、LAT、VGG、EVD、NVD
	Case11	LON、LAT、GA、VGG、EVD、NVD

wavelength gravity anomaly (RSG), residual long-wavelength gravity anomaly (RLG), gravity anomaly (GA), vertical gravity gradient (VGG), east-west vertical deviation (EVD), and north-south vertical deviation (NVD). A total of 12 experimental cases were designed. Cases 0–3 employ the traditional dual-channel BP neural network, while Cases 4–11 utilize the PSO-optimized dual-channel BP neural network (PSO_BP). For the BP neural network, the learning rate was set to 0.001, with all other parameters remaining unchanged.

To specifically evaluate the effectiveness of PSO optimization, four key pairs of comparisons were established: Case 0 vs. Case 4, Case 1 vs. Case 5, Case 2 vs. Case 6, and Case 3 vs. Case 11. These pairs facilitate a direct comparison of performance differences between the dual-channel BP and PSO_BP models under identical input configurations. Both Case 0 and Case 4 include comprehensive gravity data inputs—SG, LG, RSG, and RLG—enabling analysis of how PSO optimization influences prediction outcomes when utilizing residual anomalies. Other cases progressively introduce or exclude specific data types, such as VGG, EVD, and NVD, to explore the contribution of vertical deviations and gravity gradients to prediction accuracy.

This experimental design allows for a systematic assessment of two core objectives: (1) the influence of varying gravity data combinations on the accuracy of seafloor depth prediction, and (2) the extent to which PSO optimization enhances model convergence and prediction performance. Through this approach, the role of each gravity data type and optimization method in improving prediction accuracy is comprehensively analyzed, providing insights into optimal strategies for seafloor depth modeling.

Table 5 presents the statistical results from different experimental cases, focusing on the influence of varying gravity data combinations and the effectiveness of PSO optimization in enhancing prediction performance.

The analysis of Table 5 reveals that integrating diverse gravity data significantly enhances seafloor depth prediction accuracy, particularly when coupled with PSO optimization. Cases incorporating both long- and short-wavelength gravity anomalies (LG, SG) and their residuals (RLG, RSG) achieve the best performance. For instance, Case4 (PSO_BP) shows the lowest STD (25.45 m) and MAE (9.95 m), with an R^2 of 99.96 % and a reduced MAPE of 3.70 %, outperforming the non-optimized counterpart Case0 (BP) (STD of 26.05 m, MAE of 9.99 m, R^2 of 99.95 %, and MAPE of 3.90 %). This improvements confirms that comprehensive gravity inputs, enhanced by PSO, contribute to both absolute and relative accuracy gains. In contrast, cases using limited gravity data show significantly reduced performance. Case1 (BP), using GA alone, records a high STD (99.50 m), MAE (44.95 m), R^2 (99.33 %), and MAPE (9.59 %). Although PSO optimization in Case5 improves these metrics (STD: 78.99 m, MAE: 35.34 m, R^2: 99.58 %, and MAPE: 8.19 %), its performance remains inferior to cases incorporating residual components or additional gravity features. The poorest performance is observed in Case8, which uses only EVD and NVD, yielding the largest STD (112.63 m) and MAE (42.62 m), along with a relatively high MAPE (7.92 %), demonstrating the limited predictive value of vertical deviations alone.

Table 5
Statistical results of the comparison of seafloor depth predictions from different experimental cases with measured bathymetric data at NCEI validation points (Unit: m).

Method	Case	Mean	STD	RMSE	MAE	R^2/%	MAPE/%
BP	case0	−1.05	26.05	26.07	9.99	99.95	3.90
	case1	−0.49	99.50	99.50	44.95	99.33	9.59
	case2	0.29	84.63	84.63	38.95	99.51	8.52
	case3	0.65	81.58	81.59	34.53	99.57	9.76
PSO_BP	case4	0.08	25.45	25.45	9.95	99.96	3.70
	case5	−0.47	78.99	78.10	35.34	99.58	8.19
	case6	−1.47	67.79	67.80	29.70	99.69	7.17
	case7	−0.24	79.03	79.03	36.23	99.57	8.07
	case8	−0.41	112.63	112.63	42.62	99.14	7.92
	case9	−0.71	69.05	69.06	30.07	99.68	6.80
	case10	−1.23	70.30	70.31	31.36	99.66	8.16
	case11	0.09	65.53	65.53	29.41	99.71	7.16

The consistent effectiveness of PSO is evident across all case comparisons. For instance, it reduces the STD from 84.63 m (Case2) to 67.79 m (Case6), MAE from 38.95 m to 29.70 m, and MAPE from 8.52 % to 7.17 %, along with improved R^2 from 99.51 % to 99.69 %. Similarly, in Case11—combining GA, VGG, EVD, and NVD—PSO optimization yields substantial improvements over Case3 (non-optimized), lowering the MAE from 34.53 m to 29.41 m, MAPE from 9.76 % to 7.16 %, and increasing R^2 from 99.57 % to 99.71 %. These consistent gains affirm PSO's ability to suppress stochastic variability and accelerate convergence.

The contribution of different gravity data types is also evident. Comparisons between Case5 (GA only), Case7 (GA + VGG), and Case8 (EVD + NVD) show that GA alone provides better performance (Case5 MAE: 35.34 m) than when combined with VGG (Case7 MAE: 36.23 m) or when using vertical deviations alone (Case8 MAE: 42.62 m). This indicates that GA contributes more strongly to prediction accuracy, while the addition of VGG may introduce feature redundancy.

Further comparisons between Cases 6, 9, 10, and 11 reveal that the most comprehensive gravity configuration —Case11 (GA + VGG + EVD + NVD)— achieves the highest overall accuracy, with MAE of 29.41 m, R^2 of 99.71 %, and the lowest MAPE of 7.16 %. Excluding GA, as in Case10 (VGG + EVD + NVD), leads to degraded accuracy (MAE: 31.36 m, MAPE: 8.16 %), confirming GA's dominant influence. Case6 (GA + VGG) and Case9 (GA + EVD + NVD) show comparable performance across all metrics, reinforcing that GA, whether paired with VGG or vertical deviations, is essential for reducing errors.

In summary, the analysis confirms that integrating long- and short-wavelength gravity anomalies (LG, SG) and their residuals (RLG, RSG), coupled with PSO optimization, yields the most accurate and stable seafloor depth predictions. PSO consistently enhances performance by accelerating convergence, reducing both absolute and relative prediction errors, and improving robustness. Among gravity-derived inputs, GA contributes most significantly, while residuals and vertical deviation components provide additional, but secondary, enhancements. Vertical deviations alone, however, are insufficient to achieve reliable predictions.

5. Conclusions

This study introduced a PSO-optimized dual-channel BP neural network (PSO_BP) for enhancing seafloor depth prediction accuracy in the Gulf of Mexico. By integrating shipborne bathymetric data with long- and short-wavelength gravity anomalies and their residuals—the model effectively captured the nonlinear and multiscale characteristics of marine topography.

The results demonstrate that combining gravity data of different

spatial scales significantly enhances prediction performance. The dual-channel architecture, which separates long- and short-wavelength components, enables specialized feature extraction, reduces interference during training, and leverages the distinct geophysical information each anomaly type provides. Among all configurations, the full combination of gravity anomalies and their residuals achieved the best results. The PSO optimization further enhanced prediction accuracy by accelerating convergence, reducing prediction errors, and improving the model's robustness. The integration of PSO further addressed key limitations of conventional BP networks—such as slow convergence, sensitivity to initial weights, and susceptibility to local minima—by providing a robust global search mechanism. This led to improved convergence stability, reduced prediction errors, and enhanced generalization ability.

Extensive comparative experiments confirmed that the PSO_BP model consistently outperformed existing global bathymetric models (GEBCO_2024, Topo_25.1, DTU18_BAT, and SRTM15 + V2.6), achieving the lowest RMSE, MAE, and MAPE values and the highest R^2 scores across multiple depth zones and varying distances from shore. The results also reveal that gravity anomalies and their residuals are the most informative predictors, while vertical deviation data alone contribute less to accuracy.

Despite its strong performance, several limitations remain. The method has so far only been validated in the Gulf of Mexico and has not been applied at a global scale or in geologically complex regions. In addition, the influence of sparse or uneven data distribution was not fully explored and may affect prediction stability in under-sampled areas.

Future research will aim to extend the approach to broader marine domains, enhance computational efficiency, explore alternative optimization strategies, and incorporate geophysical constraints to further improve model interpretability, robustness, and scalability. These developments are expected to contribute meaningfully to the refinement of global bathymetric mapping.

CRediT authorship contribution statement

Jiajia Yuan: Writing – review & editing, Writing – original draft, Methodology, Funding acquisition. **Haoran Liu:** Writing – original draft, Visualization, Validation, Data curation. **Jianli Chen:** Writing – review & editing, Supervision, Funding acquisition. **Chen Yang:** Visualization, Validation, Data curation.

Author information

Jiajia Yuan: now at The Hong Kong Polytechnic University, Hong Kong, China.

Declaration of competing interest

The authors declare that they have no known competing financial interests or personal relationships that could have appeared to influence the work reported in this paper.

Acknowledgments

This work was supported by the Natural Science Research Project of Anhui Educational Committee (2023AH051199), Scientific Research Foundation for High-level Talents of Anhui University of Science and Technology (2022yjrc66), National Natural Science Foundation of China (NSFC) National Major Programme (42394132), Hong Kong RGC Collaborative Research Fund (C5013-23G) and PolyU SHS and LSGI Internal Research Funds (Project IDs: P0042322 & P0041486).

We extend our sincere gratitude to SIO for providing the SIO V32.1 marine gravity data model, including gravity anomaly (GA), vertical gravity gradient (VGG), and vertical deflection (VD) datasets. We also acknowledge the provision of the Topo_25.1 global seafloor topography model and the SRTM15 + V2.6 bathymetric model. Our appreciation goes to GEBCO for sharing the GEBCO_2024 global bathymetric model and to DTU for providing the DTU18_BAT global bathymetric model. Additionally, we thank NCEI under NOAA for supplying the shipborne bathymetry data used in this study.

Data availability

Data will be made available on request.

References

An, D., Guo, J., Li, Z., Ji, B., Liu, X., Chang, X., 2022. Improved gravity-geologic method reliably removing the long-wavelength gravity effect of regional seafloor topography: a case of bathymetric prediction in the south China sea. IEEE Trans. Geosci. Rem. Sens. 60, 1–12. https://doi.org/10.1109/TGRS.2022.3223047.

An, D., Guo, J.Y., Chang, X., Wang, Z., Jia, Y., Liu, X., Bondur, V., Sun, H., 2024. High-precision 1′×1′ bathymetric model of Philippine Sea inversed from marine gravity anomalies. Geosci. Model Dev. (GMD) 17, 2039–2052. https://doi.org/10.5194/egusphere-2023-2132.

Anderson, N.L., Essa, K.S., Elhussein, M., 2020. A comparison study using particle swarm optimization inversion algorithm for gravity anomaly interpretation due to a 2D vertical fault structure. J. Appl. Geophys. 179, 104120. https://doi.org/10.1016/j.jappgeo.2020.104120.

Annan, R.F., Wan, X., 2022. Recovering bathymetry of the Gulf of Guinea using altimetry-derived gravity field products combined via convolutional neural network. Surv. Geophys. 43, 1541–1561. https://doi.org/10.1007/s10712-022-09720-5.

Altinoğlu, F.F., Sari, M., Aydin, A., 2015. Detection of lineaments in Denizli Basin of Western Anatolia region using bouguer gravity data. Pure Appl. Geophys. 172, 415–425. https://doi.org/10.1007/s00024-014-0911-y.

Chen, L., Zhang, X., Yao, M., 2023. Research on short-term forecasting of power load based on improved genetic algorithm optimized BP neural network. 2023 4th International Conference on Power Engineering (ICPE), Macau, Macao, pp. 323–328. https://doi.org/10.1109/ICPE59729.2023.10468972.

Chicco, D., Warrens, M.J., Jurman, G., 2021. The coefficient of determination R-squared is more informative than SMAPE, MAE, MAPE, MSE and RMSE in regression analysis evaluation. PeerJ Comput. Sci. 7. https://doi.org/10.7717/peerj-cs.623.

Ekwok, S.E., Eldosouky, A.M., Essa, K.S., George, A.M., Abdelrahman, K., Fnais, M.S., András, P., Akaerue, E.I., Akpan, A.E., 2023. Particle swarm optimization (PSO) of high-quality magnetic data of the obudu basement complex, Nigeria. Minerals 13 (9), 1209. https://doi.org/10.3390/min13091209.

Essa, K.S., Géraud, Y., Diraison, M., 2021. Fault parameters assessment from the gravity data profiles applying the global particle swarm optimization. J. Petrol. Sci. Eng. 207, 109129. https://doi.org/10.1016/J.PETROL.2021.109129.

Fan, D., Li, S., Meng, S., Lin, Y., Xing, Z., Zhang, C., Yang, J., Wan, X., Qu, Z., 2020. Applying iterative method to solving high-order terms of seafloor topography. Mar. Geod. 43 (1), 63–85. https://doi.org/10.1080/01490419.2019.1670298.

Fan, D., Li, S., Li, X., Yang, J., Wan, X., 2021. Seafloor topography estimation from gravity anomaly and vertical gravity gradient using nonlinear iterative least square method. Remote Sens. 13 (1), 64. https://doi.org/10.3390/rs13010064.

Gad, A.G., 2022. Particle swarm optimization algorithm and its applications: a systematic review. Arch. Comput. Methods Eng. 29, 2531–2561. https://doi.org/10.1007/s11831-021-09694-4.

Gou, L., Shao, W., Zeng, X., Shen, Y., Zhou, Z., 2019. Rapid simulated annealing algorithm for optimization of aeroengine control based on BP neural network. In: 2019 Chinese Control Conference (CCC), pp. 8848–8852. https://doi.org/10.23919/ChiCC.2019.8866588. Guangzhou, China.

Ge, B., Guo, J., Kong, Q., Zhu, C., Huang, L., Sun, H., Liu, X., 2025. Seafloor topography inversion from multi-source marine gravity data using multi-channel convolutional neural network. Eng. Appl. Artif. Intell. 139 (Part A), 109567. https://doi.org/10.1016/j.engappai.2024.109567.

Harper, H., Sandwell, D.T., 2024. Global predicted bathymetry using neural networks. Earth Space Sci. 11, e2023EA003199. https://doi.org/10.1029/2023EA003199.

Hodson, T.O., 2022. Root-mean-square error (RMSE) or mean absolute error (MAE): when to use them or not. Geosci. Model Dev. (GMD) 7 (3), 1247–1250. https://doi.org/10.5194/gmd-15-5481-2022.

Hsiao, Y., Hwang, C., Cheng, Y., Chen, L., Hsu, H., Tsai, J., Liu, C., Wang, C., Liu, Y., Kao, Y., 2016. High-resolution depth and coastline over major atolls of South China Sea from satellite altimetry and imagery. Rem. Sens. Environ. 176, 69–83. https://doi.org/10.1016/J.RSE.2016.01.016.

Huang, Y., Xiang, Y., Zhao, R., Cheng, Z., 2020. Air quality prediction using improved PSO-BP neural network. IEEE Access 8, 99346–99353. https://doi.org/10.1109/ACCESS.2020.2998145.

Ibrahim, A., Hinze, W., 1972. Mapping buried bedrock topography with gravity. Ground Water 10 (3), 18–23. https://doi.org/10.1111/j.1745-6584.1972.tb02921.x.

Kennedy, J., Eberhart, R., 2002. Particle swarm optimization. In: Proceedings of ICNN'95 - International Conference on Neural Networks, pp. 1942–1948. https://doi.org/10.1109/ICNN.1995.488968. Perth, WA, Australia.

Li, D., Zhao, Z., 2022. Facet-based hybrid method for electromagnetic scattering from shallow water waves modulated by submarine topography. IEEE Trans. Geosci. Rem. Sens. 60, 1–14. https://doi.org/10.1109/TGRS.2022.3164992.

Li, H., 2022. Application of PSO-BP neural network in GPS height fitting. 2022 IEEE 2nd International Conference on Power, Electronics and Computer Applications (ICPECA), Shenyang, China, pp. 532–536. https://doi.org/10.1109/ICPECA53709.2022.9718911.

Mehfuz, S., Kumar, S., 2014. Two dimensional particle swarm optimization algorithm for load flow analysis. Int. J. Comput. Intell. Syst. 7 (6), 1074–1082. https://doi.org/10.1080/18756891.2014.963973.

Sandwell, D.T., Smith, W.H.F., 2009. Global marine gravity from retracked Geosat and ERS-1 altimetry: ridge segmentation versus spreading rate. J. Geophys. Res. Solid Earth 114 (B1), B01411. https://doi.org/10.1029/2008JB006008.

Sandwell, D.T., Müller, R.D., Smith, W.H.F., Garcia, E., Francis, R., Tregoning, P., 2014. New global marine gravity model from CryoSat-2 and Jason-1 reveals buried tectonic structure. Science 346 (6205), 65–67. https://doi.org/10.1126/science.1258213.

Sagawa, T., Yamashita, Y., Okumura, T., Yamanokuchi, T., 2019. Satellite derived bathymetry using machine learning and multi-temporal satellite images. Remote Sens. 11, 1155. https://doi.org/10.3390/rs11101155.

Song, Z.W., Xu, J., Zhen, Y., Jiang, J., 2023. Research on clock holding technology based on PSO-BP neural network. In: 2023 4th International Conference on Electronic Communication and Artificial Intelligence (ICECAI),, pp. 331–335. https://doi.org/10.1109/ICECAI58670.2023.10176753. Guangzhou, China.

Sun, H., Feng, Y., Fu, Y., Sun, W., Peng, C., Zhou, X., Zhou, D., 2022. Bathymetric prediction using multisource gravity data derived from a parallel linked BP neural network. J. Geophys. Res. Solid Earth 127 (11), e2022JB024428. https://doi.org/10.1029/2022JB024428.

Smith, W.H.F., Sandwell, D.T., 1997. Global seafloor topography from satellite altimetry and ship depth soundings. Science 277 (5334), 1956–1962. https://doi.org/10.1126/science.277.5334.1956.

Vrigazova, B., 2021. The proportion for splitting data into training and test set for the bootstrap in classification problems. Business Sys. Res. J. 12, 228–242. https://doi.org/10.2478/bsrj-2021-0015.

Wu, C., Su, X., Xu, C., Jian, G., Li, J., 2024. Seafloor topography refinement from multi-source data using genetic algorithm - backpropagation neural network. Geophys. J. Int. 238 (3), 1417–1428. https://doi.org/10.1093/gji%2Fggae229.

Xi, R., Lv, L., Yan, X., 2024. Multi-Beam line measurement model based on analytic geometry. Highlights Sci., Eng. Technol. 85, 52–58. https://doi.org/10.54097/v2r6k082.

Xiang, X., Wan, X., Zhang, R., Li, Y., Sui, X., Wang, W., 2017. Bathymetry prediction with the gravity-geologic method: a study of long-wavelength gravity modeling based on adaptive mesh. Mar. Geod. 40 (5), 329–340. https://doi.org/10.1080/01490419.2017.1335257.

Xu, C., Li, J., Jian, G., Wu, Y., Zhang, Y., 2023. An adaptive nonlinear iterative method for predicting seafloor topography from altimetry-derived gravity data. J. Geophys. Res. Solid Earth 128 (1), e2022JB025692. https://doi.org/10.1029/2022JB025692.

Yang, J., Jekeli, C., Liu, L., 2018. Seafloor topography estimation from gravity gradients using simulated annealing. J. Geophys. Res. Solid Earth 123 (8), 6958–6975. https://doi.org/10.1029/2018JB015883.

Yang, L., Liu, M., Liu, N., Guo, J., Lin, L., Zhang, Y., Du, X., Xu, Y., Zhu, C., Wang, Y., 2023. Recovering bathymetry from satellite altimetry-derived gravity by fully connected deep neural network. IEEE Geosci. Remote Sens. Lett. 20, 1–5. https://doi.org/10.1109/LGRS.2023.3302992.

Yuan, J., Yang, C., Dong, D., Guo, J., An, D., Yu, D., 2025. Seabed depth prediction using multi-scale gravity anomalies and fully connected deep neural networks: a novel approach applied to the south China sea. Remote Sens. 17, 412. https://doi.org/10.3390/rs17030412.

Zhang, Y., Xu, H., Li, Y., Lin, G., Zhang, L., Tao, C., Wu, Y., 2024. An integer-fractional gradient algorithm for back propagation neural networks. Algorithms 17 (5), 220. https://doi.org/10.3390/a17050220.

Zhou, S., Liu, X., Guo, J., Jin, X., Yang, L., Sun, Y., Sun, H., 2023. Bathymetry of the Gulf of Mexico predicted with multilayer perceptron from multisource marine geodetic data. IEEE Trans. Geosci. Rem. Sens. 61, 4208911. https://doi.org/10.1109/TGRS.2023.3328035.

Zhou, S., Liu, X., Sun, Y., Chang, X., Jia, Y., Guo, J.Y., Sun, H., 2024. Predicting bathymetry using multisource differential marine geodetic data with multilayer perceptron neural network. Int. J. Digi. Earth 17 (1), 2393255. https://doi.org/10.1080/17538947.2024.2393255.

Zong, J., Bian, S., Tong, Y., Ji, B., Li, H., Xi, M., 2022. Classification of gravity matching areas using PSO-BP neural networks based on PCA and satellite altimetry data over the western pacific. Sensors 22 (24), 9892. https://doi.org/10.3390/s22249892.